Fine spectroscopy and Judd-Ofelt analysis of Pr3+ doped Sr0.7La0.3Mg0.3Al11.7O19 (Pr:ASL)

Suchinda Sattayaporn, Pascal Loiseau, Gerard Aka, Sergei Klimin, Kirill Boldyrev, Boris Mavrin

Fine spectroscopy and Judd-Ofelt analysis of Pr^{3+} doped $Sr_{0.7}La_{0.3}Mg_{0.3}Al_{11.7}O_{19}$ (Pr:ASL)

Suchinda Sattayaporn[a,b], Pascal Loiseau[b*], Gerard Aka[b], Sergei Klimin[c], Kirill Boldyrev[c] and Boris Mavrin[c]

(a) Synchrotron Light Research Institute (Public Organization), 30000, Nakhon Ratchasima, Thailand
(b) Chimie ParisTech, PSL Research University, CNRS, Institut de Recherche de Chimie Paris, 75005 Paris, France.
(c) Institute of Spectroscopy RAS, Moscow, Troitsk 148880, Russia

- Email address of corresponding author : pascal.loiseau@chimieparistech.psl.eu
- Tel number: +33 (0)1 85 78 42 40

Abstract

Single crystals of Pr^{3+} doped hexa-aluminate $Sr_{0.7}La_{0.3}Mg_{0.3}Al_{12}O_{19}$ (ASL) were prepared for spectroscopic characterization. We investigated their optical spectroscopic properties in σ and π polarization of light. Absorption spectra were recorded in extended spectral range, 400 nm – 5400 nm. Energies of Pr^{3+} crystal field states were determined. In addition to the major D_{3h} sites, minor sites were found. Judd-Ofelt analysis was performed: the J-O parameters Ω_t were determined to be 1.06×10^{-20} cm^{-2}, 2.31×10^{-20} cm^{-2} and 3.43×10^{-20} cm^{-2} for t = 2, 4 and 6, respectively. The radiative lifetime was 38 µs for the emitting state $^3P_0$.

Keywords: *visible solid state laser, high resolution spectroscopy, praseodymium, Judd-Ofelt analysis*

1. Introduction

High-power solid-state laser sources in the visible spectral range are interesting for various applications such as display technology, submarine communication, scientific spectroscopy, and biomedical treatment. Among lanthanide ions, Pr^{3+} is attractive dopant ion by possessing many transitions in the visible spectral range from 400 nm to 800 nm [1].

It is many years Pr^{3+} doped fluoride and oxide single crystals have been grown and thoroughly investigated for their optical properties and laser performances [2,3,4,5]. Although some fluoride hosts exhibit advantages of weak crystal field and low maximum phonon energy which lead to high visible laser efficiencies, there have drawbacks such as complications of crystal growth. On the other hand, a good compromise of thermo-mechanical and radiative properties can be found in some Pr^{3+} doped oxide hosts, for instance $YAlO_3$ (YAP) [6], $CaAl_{12}O_{19}$ (CAlO) [7], $LaMgAl_{11}O_{19}$ (LMA) [8,9], $SrAl_{12}O_{19}$ (SRA) hexaaluminates [10] and $SrLaGa_3O_7$ (SLGM) [11] melilite. Furthermore, all of them can be easily grown by using conventional Czochralski method. According to recent works [1,10], satisfying laser efficiencies were achieved with Pr:SRA. However, the as-grown Pr:SRA crystals contained several defects such as inclusions and cracks due to its non-congruent melting behavior [12]. It is challenging to modify its melting behavior for the optimization of optical quality. Partial co-doping of La ions into SRA host could help for this purpose by considering that isostructural LMA has congruent melting behavior [9]. The solid solution with chemical composition of $Sr_{1-x}La_xAl_{12-x}Mg_xO_{19}$ is so-called ASL. According to previous works [13,14], the composition of x=0.3 leads for instance to quasi-congruent behavior and to better crystal quality. For this work, we grew large-size Pr:ASL single crystals by Czochralski method and performed several spectroscopic characterizations including ground state absorption, optical emission and Judd-Ofelt analysis for a large covered spectral region from visible to near-infrared (NIR). One of the objective of this work is to investigate how the structure modification from SRA to ASL influences the spectroscopic properties of Pr^{3+} doping ions.

2. Crystal preparation

$Sr_{1-x}La_xAl_{12-x}Mg_xO_{19}$ (ASL) belongs to hexagonal system with space group $P6_3/mmc$ and is isomorphic to SRA. Thus, it has the magnetoplumbite structure, consisting of spinel blocs and mirror plane (001) as depicted in Figure 1. As ASL is a solid solution between SRA and LMA, La^{3+} cations ideally occupy randomly the same crystallographic sites as Sr^{2+} ions. These sites lie in mirror planes with ideal D_{3h} symmetry that Pr^{3+} doping ions are expected to occupy too. Nevertheless, some distortion of this site may lead to symmetry lowering like C_{3v} or C_{2v} [15,16].

The crystal growth of ASL doped with 2.0 at.% Pr were carried out under N_2 atmosphere by using an iridium crucible (ø50 mm × 50 mm). The growth process was carried out with a $\vec{c}$-axis cut Pr:ASL seed. We reported the resulting ASL boule in a recently published paper [17]: it was free from inclusion and crack, with good optical qualities, although a core defect was observed along the center with diameter of 1 - 2 mm. Since ASL is uniaxial crystal, the spectroscopic properties must be investigated for light polarized perpendicular (σ) and parallel (π) to the $\vec{c}$-axis. Pr:ASL samples were oriented, cut and polished perpendicularly to their $\vec{a}$ -axis and $\vec{c}$-axis with lengths of 6 mm and 5 mm, respectively.

3. Experimental

IR-reflectivity spectra were measured with a Bruker IFS66 Fourier-spectrometer and Raman spectra with a Renishaw inVia spectrometer.

Energy level diagram of Pr^{3+} ion was built using temperature-dependent measurements of both transmission and luminescent spectra. For this purpose, we used a Bruker IFS125HR Fourier-spectrometer equipped with optical closed-cycle helium cryostat based on CRYOMECH PT403 pulse-tube cryo-refrigerator. In the case of luminescence experiments, a home-made unit was used and excitation was achieved with a 450-nm laser diode.

For Judd-Ofelt analysis, the ground state absorption (GSA) spectra were recorded for σ- and π-polarized light at RT in the extended spectral range 400-1700 nm. The absorption measurements were performed with a spectral resolution of 0.2 nm by using a Varian Cary 5000 UV-VIS-IR spectrophotometer.

4. Spectroscopic analysis

3.1 Infrared spectroscopy

IR-reflectivity spectra were measured for two polarizations and compared to Raman spectra (non polarized) in Figure 2.

From both Raman and IR-active lattice vibrations, the maximum phonon energy of Pr:ASL was determined around 900 cm^{-1}. This result is in good agreement with that published earlier [17] and support the selection of ASL as laser host for Pr^{3+} ions: the gap between $^3P_0$ emitting level and $^1D_2$ lower lying multiplet is then more than 4 times the highest phonon energy of ASL host what preserves from deleterious multiphonon relaxation.

3.2 Energy level diagram

Transmission spectra at T = 5 K for Pr^{3+} IR and visible multiplets are shown in Figure 3. When interpreting the transmission spectra in the region of electronic transitions of Pr^{3+} ion in ASL:Pr, we refer to the spectroscopic study of SRA:Pr [18]. Both crystals have the same crystal structure, the site(s) for the doping ion is expected to be similar at first. Nevertheless, there is a difference because ASL matrix results from a solid solution. The formation of non-equivalent centers (NEC) for the doping ion is expected. NEC is characterized by different surrounding of praseodymium in the second coordination sphere, which leads to slight differences of the crystal field (CF) and complex lineshapes. Examples of spectral peculiarities related to the NECs in solid solutions can be found in, e.g., Refs. [19,20], where complex lineshape with total splitting of the spectral line due to the NECs up to 10 cm^{-1} was registered in mixed RE nickelates $(RE^1_xRE^2_{1-x})_2BaNiO_5$.

In Figure 3, all the most significant lines in GSA spectra of Pr:ASL are marked by ticks at the top of each panel together with drop dashed lines. In the sites with D_{3h} symmetry the CF levels of non-Kramers ion can have singlet Γ_1, Γ_2, Γ_3, and Γ_4 or doublet Γ_5 and Γ_6 states. The number of CF levels and their irreducible representations for Pr^{3+} ion in D_{3h} site are given in Table 1, while selection rules for electro-dipole (ED) transitions are given in Table 2.

In accordance with conclusion of Ref. [18], we derived that the ground state of $^3H_4$ is Γ_6 for Pr^{3+} ion in ASL. Actually, in the transmission spectra corresponding to the $^3H_4 \rightarrow {}^3P_0$ transition there is only σ-polarized line at 5K. The only CF level of $^3P_0$ multiplet has Γ_1 symmetry and the only possibility to observe σ-polarized absorption is that ground state is Γ_6 (see Table 1 and Table 2). From this, one can calculate the number of spectral lines in each multiplet for the allowed ED transitions from the ground Γ_6 level. The result of such a calculation with the

use of selection rules is given in the last column of Table 1. Calculated numbers correspond to the low-temperature spectra at 5 K, as only the ground state of $^3H_4$ is significantly populated at this low temperature.

The number of experimental lines found in multiplets at 5 K exceeds that expected from the analysis given above. For example, in the $^3H_4 \rightarrow {}^1G_4$ transition we observe three strong σ-polarized lines as expected and several additional weaker lines separated by rather big distance of the order of 100 cm^{-1}. The same occurs for the π-polarized lines, where only one line is allowed according to the selection rules for D_{3h} site. Such weaker peaks, observed in all multiplets, are attributed to Pr^{3+} ions in minority sites with symmetry differing from D_{3h}. For instance they could arise from Pr^{3+} in off-centered sites around the three-fold axis: the resulting site symmetry is then C_{2V} as it was already proposed in LMA [16]. C_{3V} can arise from Pr^{3+} ion displacement along the threefold axis or from the neighborhood of Mg^{2+} ion in the second coordination shell breaking the mirror symmetry around Pr^{3+} ion.

Moreover, some spectral lines have complex lineshapes, like σ-polarized line in the $^3H_4 \rightarrow {}^3F_2$ transition (Figure 3): while only two ED transitions are allowed for the D_{3h} site, this line can be fitted by three independent lorentzians, separated by distances of the order of 10 cm^{-1}. Such a lineshape could arise from the presence of NECs due to different site occupation in the second coordination shell. For a given center in a solid solution, a number of different configurations in the nearest surrounding occurs, which leads to a variation of a crystal field and, finally, to a shift of a spectral line [21].

Figure 4 shows transmission spectra in the region of the praseodymium $^3H_4 \rightarrow {}^3F_4$ intermultiplet transition at various temperatures together with the scheme of transitions. At higher temperatures than 5K, one can populate the excited levels of the ground $^3H_4$ multiplet. Noteworthy, the thermal population of the ground CF level diminishes as well as the intensities of the corresponding transitions originating from this ground level. Populated excited levels allow new transitions in the spectra marked by dashed arrows in the scheme of transitions in Figure 4 (d). Analysis of the high-temperature ("hot") transitions enables the determination of an energy diagram for the ground praseodymium multiplet.

Table 3 summarizes the energies of the electronic transitions of Pr^{3+} ion in ASL crystal. The number of levels in each multiplet exceeds that for the D_{3h} site as the data on all the energies found in a crystal is presented including minor sites and NECs.

The interpretation of the transmission spectra in the region of electronic transitions of Pr^{3+} ion in ASL are in accordance with that proposed for the mentioned isostructural crystal Pr:SRA [18]. The common features in both matrices are as follows: (1) most of Pr^{3+} ions occupy D_{3h} sites so that the number and polarization dependence of the most intense lines are in coincidence between ASL and SRA; (2) there are evidences for additional praseodymium minor sites which could correspond to sites with C_{2V} or C_{3V} symmetry [16]. Nevertheless, in Pr:ASL crystal, we have found specific splittings of several spectral lines attributed to the presence of the NECs, which are distinctive features of the solid solutions.

The energy diagram built by analyzing transmittance temperature-dependent (TD) spectra was further checked in consistence with the luminescence TD spectra. Figure 5 presents the emission spectra of Pr:ASL crystal in two spectral regions at two temperatures (RT and 9 K) as well as color maps in the wavenumber-temperature coordinates. At RT the intensity of the luminescent spectra are much higher than that at 9 K due to the more effective excitation at RT. We use the data from Table 3 to calculate the frequencies of the luminescent transitions. They are depicted at the top of Figure 5 as bars accompanied by drop lines. Black bars denote the transitions starting from the lowest levels of the initial multiplet of the transition. For example, the black bars for the transitions denoted as $^1D_2 \rightarrow {}^3F_3$ in Figure 5 (a), refer to the transitions from only the lowest CF level of the $^1D_2$ multiplet, i.e., the CF level at 16861 cm^{-1} (see Table 1). Thus, black bars denote luminescent transitions which take place at low temperatures as only the lowest CF levels of emitting multiplets are populated. Gray bars denote transitions occurring at elevated temperatures, which are the transitions from the excited CF levels of emitting multiplets. In the case of $^3P_0$ emitting multiplet, consisting of only one CF level, the $^3P_1+{}^1I_6+{}^3P_2$ multiplet play the role of "excited CF levels" of $^3P_0$ as the energy distance between this CF levels is small enough for one-phonon depopulation of excited states.

So, the luminescent lines shown in Figure 5 (a-d) were fully identified using the energy level scheme from Table 1, thus, confirming the reliability of the scheme.

5. Judd-Ofelt analysis

Figure 6 shows the GSA cross section spectra of Pr:ASL recorded at room temperature in the extended visible-infrared spectral range. The absorption cross section of Pr:ASL depends strongly on the polarization of light. Notably, Pr:ASL exhibits higher GSA cross sections in the σ-polarization. Such characteristics are observed also for other rare earth ions (e.g. Nd^{3+} [14]) doped in hexaaluminate hosts.

From the recorded GSA spectra at RT, experimental data of transitions were determined to perform Judd-Ofelt analysis: mean wavelength and oscillator strength. For ASL host, the determination of refractive index was reported in the literature [13]. Then, oscillator strength can be calculated with Eq 2 [22].

$$f_{exp} = \frac{4\varepsilon_0 mc^2}{10^2 e^2} \times \int \sigma_{abs}(\bar{\nu}) d\bar{\nu} \approx 1.1296 \times 10^{12} \times \int \sigma_{abs}(\bar{\nu}) d\bar{\nu} \qquad \text{Eq. 2}$$

Where m is the electron mass, e is the electron charge, c is the speed of light, all three given in SI units. $\sigma_{abs}(\bar{\nu})$ is the absorption cross section in units of cm^2 and $\bar{\nu}$ is wavenumber in units of cm^{-1}. Since ASL and SLGM are uniaxial crystal, the absorption data must be averaged over all the polarizations to better satisfy the required conditions of Judd-Ofelt theory. Thus, the mean absorption data was calculated by summing the two-thirds of experimental values in σ-polarization and one-third of values in π-polarization.

However, there are some limitations when applying Judd-Ofelt theory with Pr^{3+} ions due to its small gap between the configurations $4f^n$ and $4f^{n-1}5d$ [23]. Many works suggested to exclude $^3H_4 \rightarrow {}^3P_2$ transition to improve the accuracy and reliability of radiative results [24,25]. Therefore, in this work, the transition $^3H_4 \rightarrow {}^3P_2$ was not taken into account. The

RELIC1.0 software developed by M. P. Hehlen [22] was used to compute Judd-Ofelt analysis with 7 ground-state transitions as shown in Table 4.

Judd-Ofelt parameters, $\Omega_{2,4,6}$, and root mean square deviation, Δrms, are shown in Table 4 and compared to that of Pr:SRA. Our results are in good accordance with Pr:SRA. This confirmed that Pr:ASL optical properties are close the one of SRA end-member. The small deviations between calculated and experimental values indicate good accuracies of our Judd-Ofelt analysis.

The J-O intensity parameters $\Omega_{2,\ 4,\ 6}$ were used to calculate the radiative properties such as emission strengths f_{ems}, transition probabilities (A), branching ratios (β), radiative lifetime (τ_{rad}) for the $^3P_1$, $^3P_0$ and $^1D_2$ multiplets (see Table 5).

For Pr(2at.%):ASL, its radiative lifetime is identical to that of Pr:SRA (38 µs) reported in the literature [26]. Moreover, the comparison of radiative and experimental lifetimes [17] of Pr(2at.%):ASL results in a very high quantum efficiency (97%), underlying the quasi absence of non-radiative relaxation at room temperature (no cross relaxation and no multiphonon relaxation for instance).

From Table 6, there are several intense transitions which can be beneficial for laser emissions in the visible spectral region, for instance $^3P_1 \rightarrow {}^3H_5$ (green), $^3P_0 \rightarrow {}^3H_4$ (blue), $^3P_0 \rightarrow {}^3H_6$ (orange), $^3P_0 \rightarrow {}^3F_2$ (red) and $^3P_0 \rightarrow {}^3F_4$ (deep red). This is supported by the laser demonstration published in [17].

6. Conclusions

Pr:ASL hexaaluminate single crystal was prepared for spectroscopic characterization. High-resolution ground-state absorption spectra revealed two inequivalent cation sites of Pr^{3+} doped in ASL host, including major and minor sites with symmetries of D_{3h} and C_{2V} or C_{3V} respectively. This leads to complex GSA lineshapes evidencing the presence of additional minor sites and non-equivalent centers for Pr^{3+} ion. The GSA absorption spectra recorded at low temperature in extended range were used to establish the energy level diagram of Pr:ASL for the first time. Moreover, the J-O parameters Ω_t were derived from the GSA spectra as

1.06×10^{-20} cm^{-2}, 2.31×10^{-20} cm^{-2} and 3.43×10^{-20} cm^{-2} where t = 2,4 and 6, respectively. The Judd-Ofelt analysis demonstrated the promising radiative properties of Pr:ASL crystal, such as long radiative lifetime of 38 μs and strong emission lines in blue ($^3P_0\rightarrow{}^3H_4$), orange ($^3P_0\rightarrow{}^3H_6$), red ($^3P_0\rightarrow{}^3F_2$) and deep red ($^3P_0\rightarrow{}^3F_4$) spectral regions. As a conclusion, Pr:ASL is a good oxide medium for visible laser development, keeping most of the radiative properties of SRA but with easier preparation as single crystal.

Acknowledgements

We acknowledge the financial support from the Ministry of Science and Technology of Thailand (MOST).

Figure Captions

Figure 1. Unit cell structure of $Sr_{1-x}La_xAl_{12-x}Mg_xO_{19}$ (left) and coordination sphere of the ideal D_{3h} site (right).

Figure 2. RT (a) Raman and (b) IR reflectivity spectra of Pr:ASL.

Figure 3. Transmission spectra of Pr:ASL at T = 5 K for σ- and π-polarized light in the spectral ranges of the praseodymium multiplets.

Table 1. The irreducible representations (IRR), the number of CF levels, and the number of allowed electro-dipole (ED) transitions from the level with Γ_6 symmetry of non-Kramers ion in a D_{3h} site for multiplets with a given total momentum *J*.

Table 2. Selection rules for ED transitions of non-Kramers ion in D_{3h} site. d_x, d_y, and d_z denotes the components of the dipole moment. Polarization state of light is indicated in brackets

Table 3. Experimental energies of CF levels for given multiplets of the Pr^{3+} ion in Pr(2at.%)ASL.

Figure 4**.** Transmission spectra of Pr:ASL crystal at various temperatures in the region of the intermultiplet transition of Pr^{3+} ion: (a,b) $^3H_4 \rightarrow {}^3F_3$ in (a) π- and (b) σ-polarizations and (c) $^3H_4 \rightarrow {}^3P_0$, σ-polarization, and (d) energy level scheme.

Figure 5**.** Emission of Pr:ASL in two spectral regions as (a,c) spectra at 9 K and at 300 K and (b,d) color maps. Black and gray bars indicate energies of transitions calculated from transmission spectra at 5 K.

Figure 6. GSA spectra of Pr:ASL at RT for σ- and π-polarized light, recorded in the visible-NIR spectral range.

Table 4. Absorption lines, refractive index *n*, experimental and calculated oscillator strengths *f* of 2.0at.%Pr:ASL.

Table 5. Intensity parameters of Pr:ASL calculated by using Judd-Ofelt theory and the corresponding root mean square deviations ΔRMS

Table 6**.** Wavelengths λ , emission oscillator strengths f_{ems}, transition probabilities A, fluorescence branching ratios β, and radiative lifetimes τ of $^3P_1$, $^3P_0$ and $^1D_2$ multiplets for Pr:ASL.

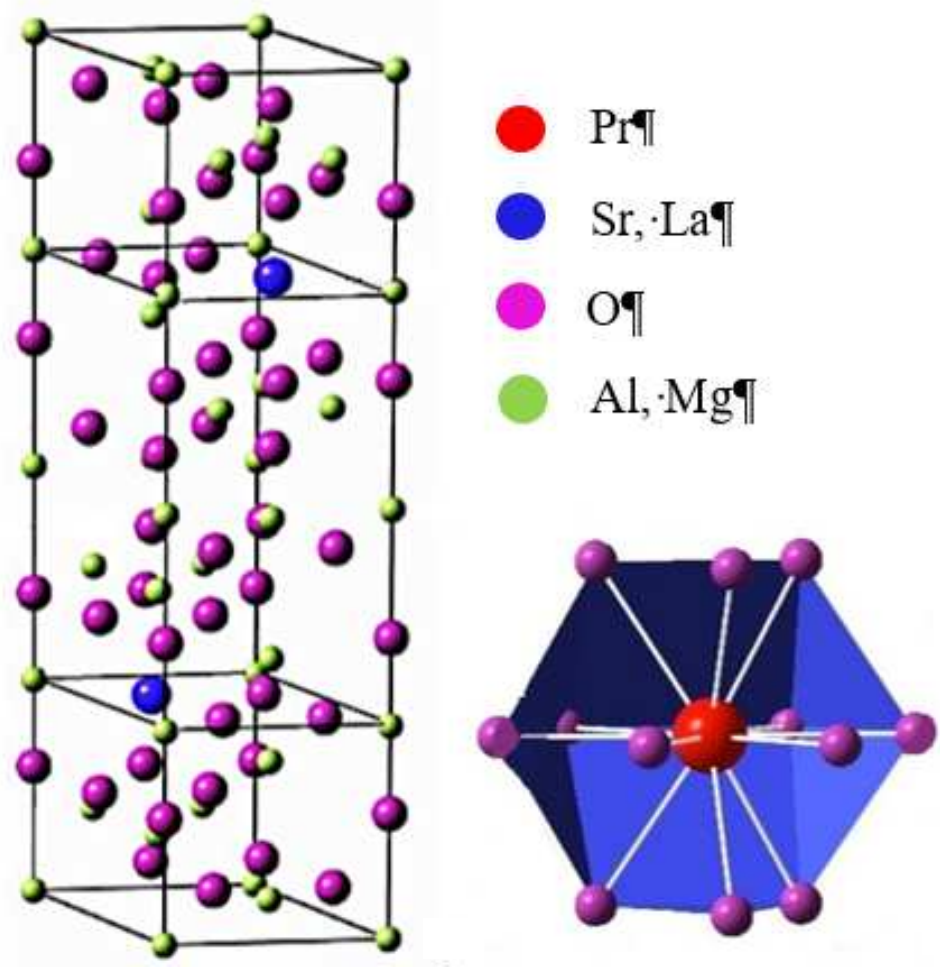

Figure 1. Unit cell structure of $Sr_{1-x}La_xAl_{12-x}Mg_xO_{19}$ (left) and coordination sphere of the ideal D_{3h} site (right).

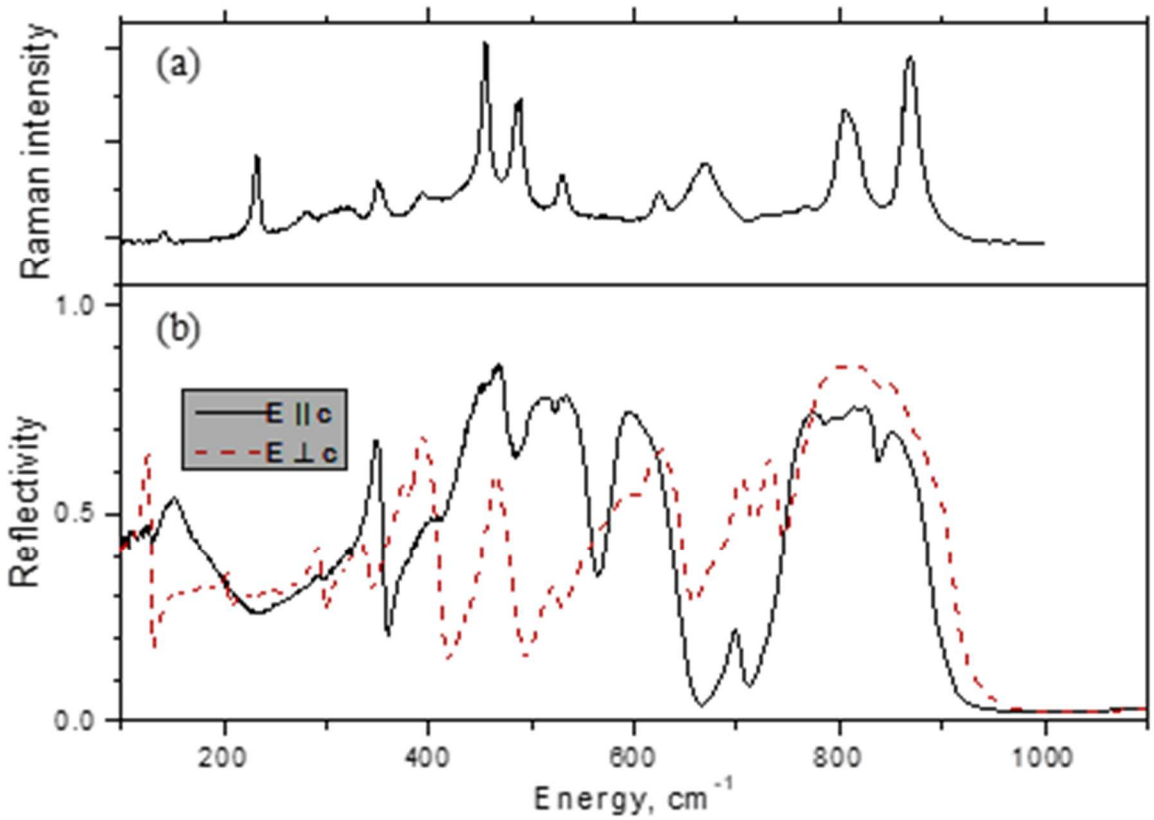

Figure 2. RT (a) Raman and (b) IR reflectivity spectra of Pr:ASL.

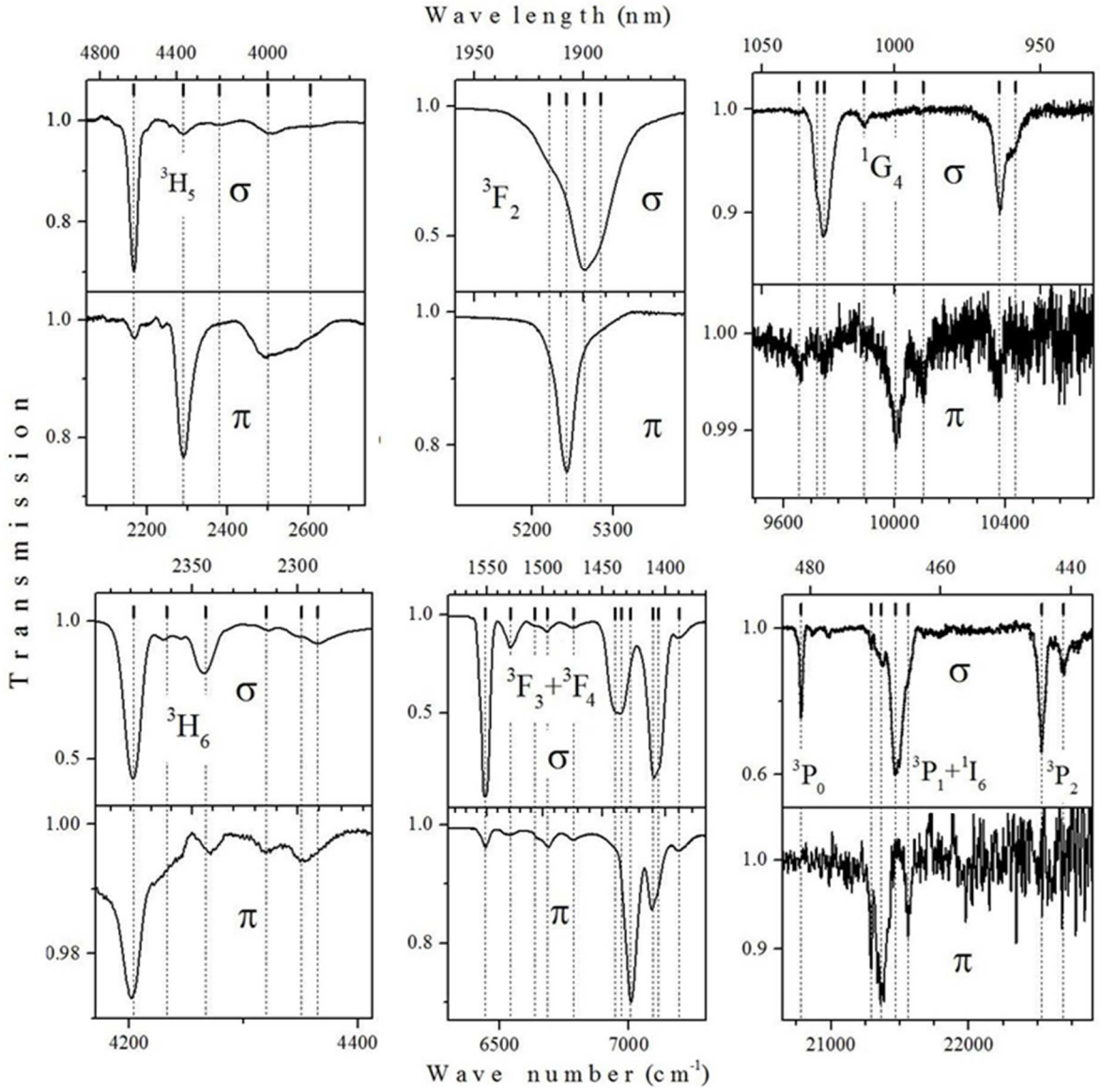

Figure 3. Transmission spectra of Pr:ASL at T = 5 K for σ- and π-polarized light in the spectral ranges of the praseodymium multiplets.

Table 1. The irreducible representations (IRR), the number of CF levels, and the number of allowed electro-dipole (ED) transitions from the level with Γ_6 symmetry of non-Kramers ion in a D_{3h} site for multiplets with a given total momentum *J*.

J	IRR's	Number of CF levels (states)	Number of ED transitions from Γ_6
0	Γ_1	1	1σ
1	$\Gamma_2 + \Gamma_5$	2(3)	1σ, 1π
2	$\Gamma_1 + \Gamma_5 + \Gamma_6$	3(5)	2σ, 1π
3	$\Gamma_2 + \Gamma_3 + \Gamma_4 + \Gamma_5 + \Gamma_6$	5(7)	2σ, 1π
4	$\Gamma_1 + \Gamma_3 + \Gamma_4 + \Gamma_5 + 2\Gamma_6$	6(9)	3σ, 1π
5	$\Gamma_2 + \Gamma_3 + \Gamma_4 + 2\Gamma_5 + 2\Gamma_6$	7(11)	3σ, 2π
6	$2\Gamma_1 + \Gamma_2 + \Gamma_3 + \Gamma_4 + 2\Gamma_5 + 2\Gamma_6$	9(13)	5σ, 2π

Table 2. Selection rules for ED transitions of non-Kramers ion in D_{3h} site. d_x, d_y, and d_z denotes the components of the dipole moment. Polarization state of light is indicated in brackets

	Γ_1	Γ_2	Γ_3	Γ_4	Γ_5	Γ_6
Γ_1			$d_z\,(\pi)$			$d_x,d_y\,(\alpha,\sigma)$
Γ_2				$d_z\,(\pi)$		$d_x,d_y\,(\alpha,\sigma)$
Γ_3	$d_z\,(\pi)$				$d_x,d_y\,(\alpha,\sigma)$	
Γ_4		$d_z\,(\pi)$			$d_x,d_y\,(\alpha,\sigma)$	
Γ_5			d_x,d_y (α,σ)	$d_x,d_y\,(\alpha,\sigma)$	$d_x,d_y\,(\alpha,\sigma)$	$d_z\,(\pi)$
Γ_6	$d_x,d_y\,(\alpha,\sigma)$	$d_x,d_y\,(\alpha,\sigma)$			$d_z\,(\pi)$	$d_x,d_y\,(\alpha,\sigma)$

Table 3. Experimental energies of CF levels for given multiplets of the Pr^{3+} ion in Pr(2at.%)ASL.

Multiplet	Energy (cm^{-1})
$^3H_4$	0, 22, 175, 195, 205, 240, 380
$^3H_5$	2167, 2290, 2379, 2492, 2507, 2611, 2730
$^3H_6$	4204, 4233, 4267, 4320, 4351, 4365
$^3F_2$	5221, 5242, 5265, 5285
$^3F_3$	6443, 6532, 6632, 6683, 6774
$^3F_4$	6947, 6971, 7007, 7081, 7092, 7116, 7187
$^1G_4$	9657, 9722, 9747, 9891, 10004, 10104, 10379, 10438
$^1D_2$	16861, 16917, 16969, 17003, 17094
$^3P_0$	20783
$^3P_1 + ^1I_6$	21289, 21365, 21468, 21561
$^3P_2$	22530, 22686

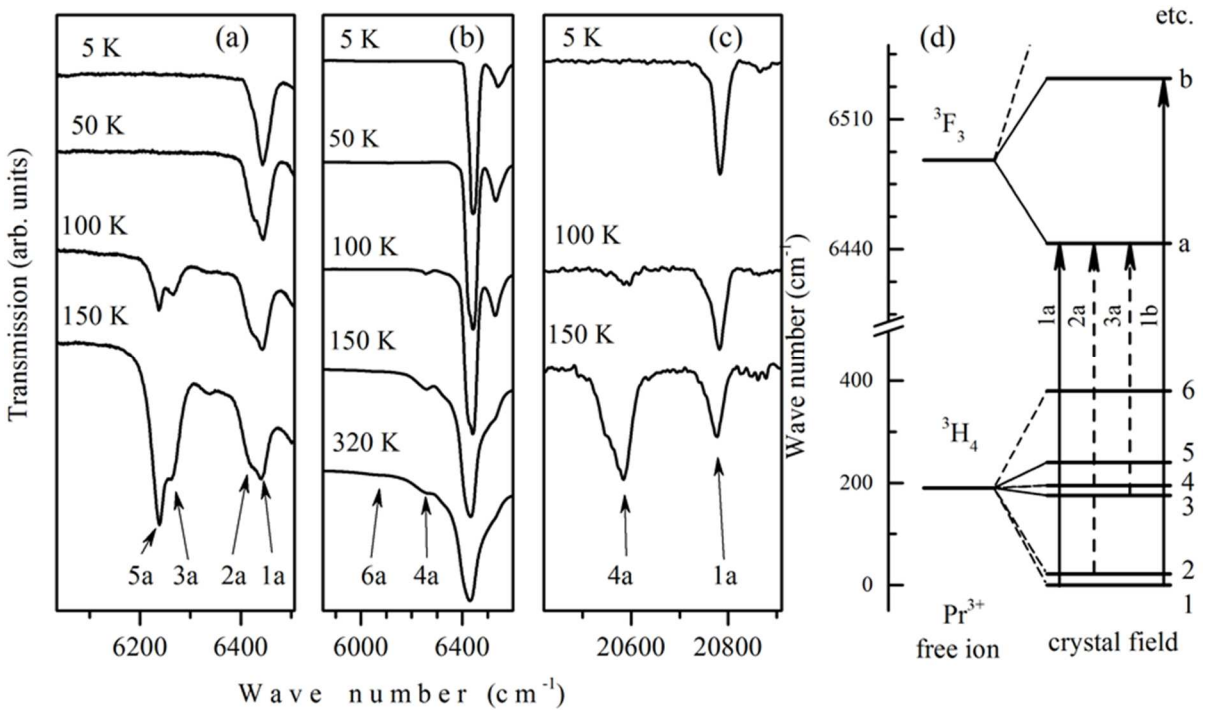

Figure 4. Transmission spectra of Pr:ASL crystal at various temperatures in the region of the intermultiplet transition of Pr3+ ion: (a,b) $^{3H4}\rightarrow^{3F3}$ in (a) π- and (b) σ-polarizations and (c) $^{3H4}\rightarrow^{3P0}$, σ-polarization, and (d) energy level scheme.

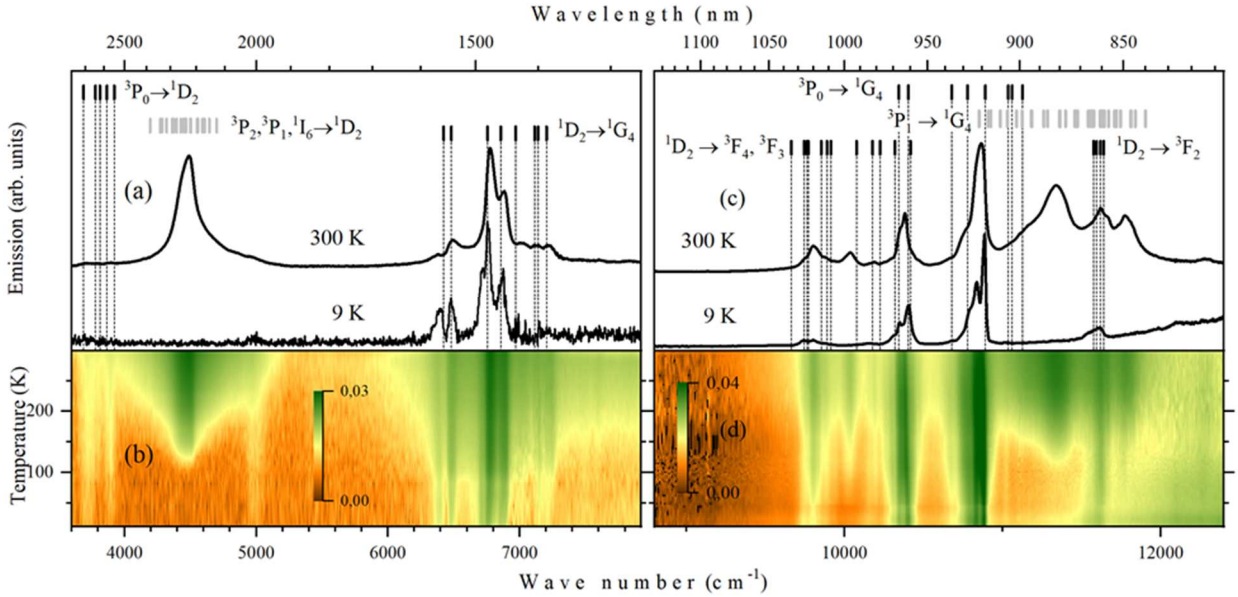

Figure 5. Emission of Pr:ASL in two spectral regions as (a,c) spectra at 9 K and at 300 K and (b,d) color maps. Black and gray bars indicate energies of transitions calculated from transmission spectra at 5 K.

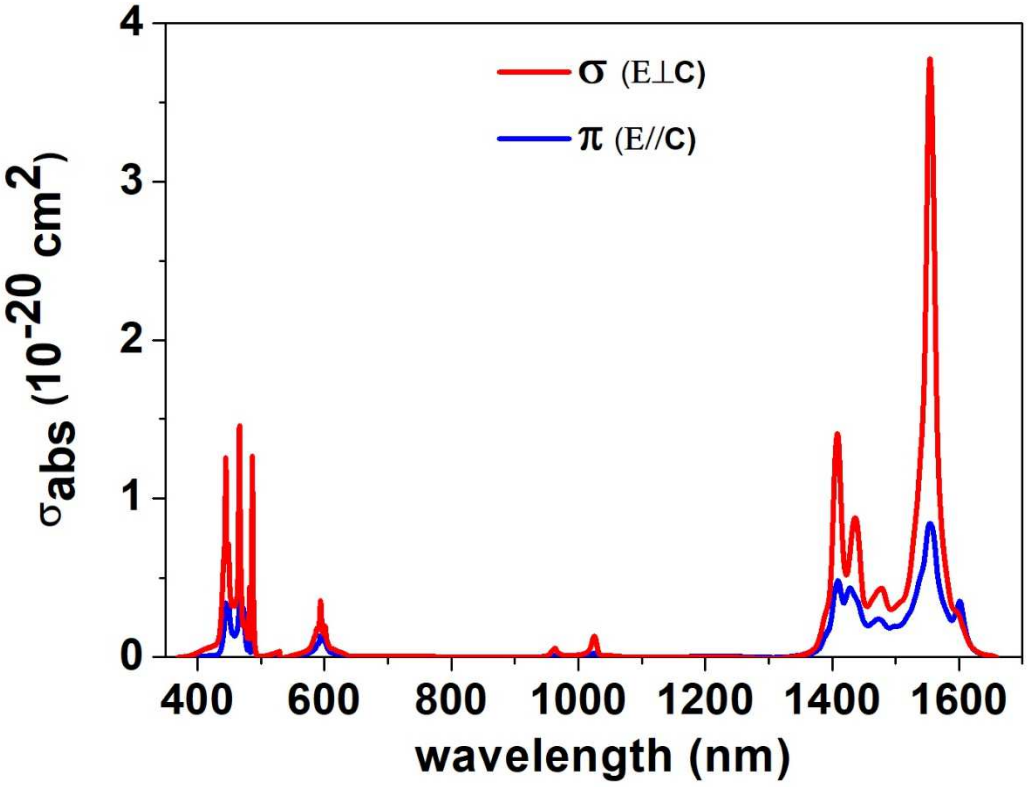

Figure 6. GSA spectra of Pr:ASL at RT for σ- and π-polarized light, recorded in the visible-NIR spectral range.

Table 4. Absorption lines, refractive index n, experimental and calculated oscillator strengths f of 2.0at.%Pr:ASL.

Transition	Wavelength (nm)	n	f_{exp} (10^{-6})	f_{cal} (10^{-6})
$^3H_4 \rightarrow {}^3P_1$	465	1.78	7.22	1.71
$^3H_4 \rightarrow {}^3P_0$	488	1.77	1.63	1.63
$^3H_4 \rightarrow {}^1D_2$	594	1.77	0.82	0.82
$^3H_4 \rightarrow {}^1G_4$	1015	1.76	0.22	0.22
$^3H_4 \rightarrow {}^3F_4$	1430	1.76	2.55	2.55
$^3H_4 \rightarrow {}^3F_3$	1557	1.76	4.17	4.17
$^3H_4 \rightarrow {}^3F_2$	1907	1.76	1.93	1.93

Table 5. Intensity parameters of Pr:ASL calculated by using Judd-Ofelt theory and the corresponding root mean square deviations ΔRMS

	Pr(2.0at.%)ASL	Pr:SRA[26]
Ω_2 (10^{-20} cm^2)	1.06	0.84
Ω_4 (10^{-20} cm^2)	2.31	2.19
Ω_6 (10^{-20} cm^2)	3.43	6.86
Δrms (10^{-20} cm^2)	0.19	0.10

Table 6. Wavelengths λ , emission oscillator strengths f_{ems}, transition probabilities A, fluorescence branching ratios β, and radiative lifetimes τ of $^3P_1$, $^3P_0$ and $^1D_2$ multiplets for Pr:ASL.

multiplet	λ	f_{ems} (10^{-6})	A	β	τ(μs)
$^3P_1 \rightarrow {}^3H_4$	458	5.03	4966	19	
$^3P_1 \rightarrow {}^3H_5$	511	11.22	8888	34	
$^3P_1 \rightarrow {}^3H_6$	580	4.37	2681	10	
$^3P_1 \rightarrow {}^3F_2$	591	2.85	1684	6	39
$^3P_1 \rightarrow {}^3F_3$	650	9.69	4738	18	
$^3P_1 \rightarrow {}^3F_4$	667	5.22	2426	9	
$^3P_1 \rightarrow {}^1G_4$	841	1.55	452	2	
$^3P_0 \rightarrow {}^3H_4$	481	15.15	14022	53	
$^3P_0 \rightarrow {}^3H_5$	537	-	-	-	
$^3P_0 \rightarrow {}^3H_6$	616	7.37	4166	16	
$^3P_0 \rightarrow {}^3F_2$	624	9.10	4952	19	38
$^3P_0 \rightarrow {}^3F_3$	691	-	-	-	
$^3P_0 \rightarrow {}^3F_4$	712	5.90	2496	9	
$^3P_0 \rightarrow {}^1G_4$	915	2.80	727	3	
$^1D_2 \rightarrow {}^3H_4$	591	1.39	836	36	
$^1D_2 \rightarrow {}^3H_5$	683	0.03	15	1	
$^1D_2 \rightarrow {}^3H_6$	813	0.76	194	8	
$^1D_2 \rightarrow {}^3F_2$	835	0.92	243	11	436
$^1D_2 \rightarrow {}^3F_3$	957	0.25	64	3	
$^1D_2 \rightarrow {}^3F_4$	995	2.66	780	34	
$^1D_2 \rightarrow {}^1G_4$	1438	1.63	157	7	

References

[1] C. Kränkel, D.-T. Marzahl, F. Moglia, G. Huber, and P. W. Metz, "Out of the blue: semiconductor laser pumped visible rare-earth doped lasers", *Laser Photon. Rev.*, **10**, 548-568 (2016). https://doi.org/10.1002/lpor.201500290.

[2] N. O. Hansen, A.-R. Bellancourt, U. Weichmann, and G. Huber, "Efficient green continuous-wave lasing of blue-diode-pumped solid-state lasers based on praseodymium-doped $LiYF_4$", *Appl. Opt.*, **49**, 3864–3868 (2010). https://doi.org/10.1364/AO.49.003864.

[3] M. Fibrich, H. Jelinkova, J. Sulc, K. Nejezchleb, and V. Skoda, "Diode-pumped Pr: YAP lasers", *Laser Phys. Lett.*, **8**, 559–568 (2011). https://doi.org/10.1002/lapl.201110025.

[4] M. Malinowski, M. Kaczkan, S. Turczyński, and D. Pawlak, "Concentration effects on Pr^{3+} luminescence in $LaAlO_3$ crystals", *Opt. Mater. (Amst.)*, **33**, 1004–1007 (2011). https://doi.org/10.1016/j.optmat.2010.11.001.

[5] P. W. Metz, K. Hasse, D. Parisi, N. O. Hansen, C. Kränkel, M. Tonelli, and G. Huber, "Continuous-wave Pr^{3+}: BaY_2F_8 and Pr^{3+}: $LiYF_4$ lasers in the cyan-blue spectral region", *Opt. Lett.*, **39**, 5158–5161 (2014). https://doi.org/10.1364/OL.39.005158.

[6] X. Lin, X. Huang, B. Liu, B. Xu, H. Xu, Z. Cai, X. Xu, D. Li, J. Liu, and J. Xu, "Continuous-wave laser operation at 743 and 753 nm based on a diode-pumped c-cut Pr:$YAlO_3$crystal", *Opt. Mater. (Amst.)*, **76**, 16–20 (2018). https://doi.org/10.1016/j.optmat.2017.12.016.

[7] F. Reichert, D.-T. Marzahl, and G. Huber, "Spectroscopic characterization and laser performance of Pr,Mg: $CaAl_{12}O_{19}$", *J. Opt. Soc. Am. B*, **31**, 349–354 (2014). https://doi.org/10.1364/JOSAB.31.000349.

[8] D.-T. Marzahl, F. Reichert, M. Fechner, N.-O. Hansen, and G. Huber, "Laser operation and spectroscopy of Pr^{3+}:$LaMgAl_{11}O_{19}$", *5th EPS-QEOD EUROPHOTON conference,* Stockholm (Sweden), paper ThP 3 (2012).

[9] H. Fan, Y. Chen, T. Yan, J. Lin, G. Peng, J. Wang, R. I. Boughton, and N. Ye, *"*Crystal growth, spectral properties and Judd-Ofelt analysis of Pr^{3+}:$LaMgAl_{11}O_{19}$*"*, *J. Alloys Compd.*, **767,** 938-943 (2018). https://doi.org/10.1016/j.jallcom.2018.07.197.

[10] F. Reichert, D. Marzahl, P. Metz, M. Fechner, N. Hansen, and G. Huber, "Efficient laser operation of Pr^{3+}, Mg^{2+} : $SrAl_{12}O_{19}$", *Opt. Lett*., **37**, 4889–4891 (2012). https://doi.org/10.1364/OL.37.004889.

[11] M. Malinowski, I. Pracka, B. Surma, T. Lukasiewicz, W. Wolifiski, and R. Wolski, "Spectroscopic and laser properties of $SrLaGa_3O_7$: Pr^{3+} crystals", *Opt. Mater. (Amst.)* **6**, 305–312 (1996). https://doi.org/10.1016/S0925-3467(96)00048-1.

[12] F. Gantis, T. Y. Chemkova, and Y. P. Udalov, "SrO-Al_2O_3 System", *Russ. J. Inorg. Chem*. **24**, 260 (1979).

[13] V. Delacarte, "Cristallogénèse et étude spectroscopique de l'aluminium de strontium lanthane $Sr_{1-x}La_xMg_xAl_{12-x}O_{19}$ (ASL) dope Nd, Cr, Nd-Cr ou Pr. Propriétés laser de l'ASL: Nd", *PhD Thesis*, Université Pierre et Marie Curie, (1994).

[14] L. Zheng, P. Loiseau, and G. Aka, "Diode-pumped laser operation at 1053 and 900 nm in $Sr_{1-x}La_{x-y}Nd_yMg_xAl_{12-x}O_{19}$ (Nd:ASL) single crystal", *Laser Phys.* **23**, 095802-095808 (2013). https://doi.org/10.1088/1054-660X/23/9/095802.

[15] P. Higel, *"*De la caractérisation de matrices cristallines hexa-aluminates et nickelates à la recherché de bistabilité optique de terres rares*"*, *PhD Thesis*, Université Pierre et Marie Curie, (2006).

[16] A. Kahn, A. M. Lejus, M. Madsac, J. Théry, D. Vivien, and J. C. Bernier, "Preparation, structure, optical, and magnetic properties of lanthanide aluminate single crystals ($LnMAl_{11}O_{19}$)", *J. Appl. Phys.*, **52**, 6864-6869 (1981). https://doi.org/10.1063/1.328680.

[17] S. Sattayaporn, P. Loiseau, G. Aka, D. MArzahl, and C. Kränkel, "Crystal growth, spectroscopy and laser performances of Pr^{3+}: $Sr_{0.7}La_{0.3}Mg_{0.3}Al_{11.7}O_{19}$ (Pr :ASL)", *Opt. Express*, **26**, 15932–15941 (2018). https://doi.org/10.1364/OE.26.001278.

[18] B. Zandi, L.D. Merkle, J.B. Gruber, D.E. Wortman, and C.A. Morrison, "Optical spectra and analysis for Pr^{3+} in $SrAl_{12}O_{19}$", *J. Appl. Phys.* **81**, 1047–1054 (1997). https://doi.org/10.1063/1.363886.

[19] M.N. Popova, S.A. Klimin, P. Higel, and G. Dhalenne, "Magnetic ordering of the mixed-spin chain nickelate $(Er_{0.25}Gd_{0.75})_2BaNiO_5$: spectroscopic study", *Phys. Lett. A*, **354**, 487-491 (2006). https://doi.org/10.1016/j.physleta.2006.01.082.

[20] M.V. Narozhnyy, S.A. Klimin, E.A. Popova, and G. Dhalenne, "Evidences for non-equivalent centers in mixed chain nickelates $(Nd_xY_{1-x})_2BaNiO_5$", *J. Rare Earth.*, **27**, 603-606, (2009). https://doi.org/10.1016/S1002-0721(08)60297-5.

[21] A. Lupei, V. Lupei, C. Gheorghe, L. Gheorghe, D. Vivien, G. Aka, and E. Antic-Fidancev, "Disorder effects in Nd^{3+}-doped strontium hexa-aluminate laser crystals", *J. Phys.: Condens. Matter* **18**, 597–611 (2006). https://doi.org/10.1088/0953-8984/18/2/017.

[22] M. P. Hehlen and M. G. Brick, "50th Anniversary of the Judd-Ofelt theory : an experimentalist's view of the formalism and its application", *J. Lumin.* **136**, 221–239 (2013). https://doi.org/10.1016/j.jlumin.2012.10.035.

[23] B.E. Bowlby and B.D. Bartolo, "Applications of the Judd-Ofelt theory to the praseodymium ion in laser solids", *J. Lumin.*, **100**, 131–139 (2002). https://doi.org/10.1016/S0022-2313(02)00451-9.

[24] R. Hakim, K. Damak, A. Toncelli, M. Fourati, and R. Maalej, "Growth, optical spectroscopy and Judd–Ofelt analysis of Pr-doped BaY_2F_8 monocrystals", *J. Lumin.*, **143**, 233–240 (2013). https://doi.org/10.1016/j.jlumin.2013.04.033.

[25] F. Zhang, Z. Bi, A. Huang, and Z. Xiao, "Luminescence and Judd–Ofelt analysis of the Pr^{3+} doped fluorotellurite glass," *J. Lumin.*, **160**, 85–89 (2015). https://doi.org/10.1016/j.jlumin.2014.11.047.

[26] L. D. Merkle, B. Zandi, R. Moncorge, Y. Guyot, H. R. Verdun, and B. McIntosh, "Spectroscopy and laser operation of Pr, Mg:$SrAl_{12}O_{19}$," *J. Appl. Phys.*, **79**, 1849–1856 (1996). https://doi.org/10.1063/1.361085.